Correlative X-ray and neutron tomography of root systems using cadmium fiducial markers

Thomas Clark[1,], Genoveva Burca[2], Richard Boardman[1], Thomas Blumensath[1]

[1]University of Southampton, Southampton, SO17 1BJ, UK

[2]STFC, Rutherford Appleton Laboratory, ISIS Facility, Harwell, OX11 0QX, UK

Contact: tjc3g13@soton.ac.uk, thomas.blumensath@soton.ac.uk

Abstract

The interactions between plant roots and soil are an area of active research, particularly in terms of water and nutrient uptake. Since non-invasive, *in vivo* studies are required, tomographic imaging appears an obvious method to use, but no one imaging modality is well suited to capture the complete system. X-ray imaging gives clear insight to soil structure and composition, however water is comparatively transparent to X-rays and biological matter also displays poor contrast with respect to the pores between soil particles. Neutron imaging presents a complementary view where water and biological matter are better distinguished but the soil minerals are not imaged as clearly as they would be with X-rays.

This work aims to develop robust methods for complementary X-ray/neutron tomographic imaging of plant root samples which should lead to new insight into water and nutrient transport in soil. The key challenges of this project are to develop experiments that will meet the requirements of both imaging modalities as well as the biological requirements of the plant samples and to develop ways to register a pair of reconstructed volume images of a sample that will typically have been produced with entirely separate facilities. The use of cadmium fiducial markers for registration has been investigated. Simulations were conducted to investigate the expected registration accuracy as the quantity and distribution of the markers varied. The findings of these simulations were then tested experimentally as plant samples were grown and imaged using neutrons with the IMAT instrument at ISIS Neutron and Muon Source at the STFC Rutherford Appleton Laboratory in Harwell, and with X-rays at μ-VIS X-ray Imaging Centre at the University of Southampton.

Lay Description

The interactions between plant roots and soil are an area of active research, particularly in terms of water and nutrient uptake. The samples used in this research are typically imaged so that they can be studied without digging up the roots and destroying the sample in the process. X-ray and neutron imaging techniques have both been used as each can show different materials within the sample. Since neither can show all the components of the system by itself, this work explores methods for combining scans of the same sample to give a more complete image of the system. In particular this work focusses on the use of fiducial markers as a strategy for preparing the samples in such a way that the resulting images can be aligned. The effectiveness of this method was tested in simulation and then in practice. The samples used within this work were imaged using neutrons on the IMAT

instrument at ISIS Neutron and Muon Source at the STFC Rutherford Appleton Laboratory in Harwell, and with X-rays at μ-VIS X-ray Imaging Centre at the University of Southampton.

1   Introduction

The human race is dependent upon plants to provide all food, either directly or indirectly. As the earth's population increases, a corresponding growth in crop yield is required. Recent estimates state that crop production will need to double by 2050 in order to keep pace with projected population growth [1], a target that is not predicted to be achieved by current growth projections [2]. Climate change will make this all the more difficult, in particular through reduced water availability and the drive to reduce fertiliser usage [3]. The *green revolution* is the name given to a period in the mid twentieth century when a number of scientific advancements, including the introduction of fertilisers and genetic modification, led to a tremendous gain in crop yields in a relatively short period of time [4]. The green revolution was primarily centred on the manipulation of the portion of the plant that is visible above the ground and roots were largely overlooked. The root system is central to plant functions such as water and nutrient uptake, anchorage and interaction with symbiotic organisms and so it has been recognised that root growth and development could be further exploited to maximise crop yield [5]. It has been suggested that the deployment of crops with more efficient water and nutrient uptake due to improved traits below the ground could lead to a second green revolution and help to address the world wide challenge of food security [6].

Non-invasive, *in vivo* studies of plant roots present a challenge that has traditionally been addressed through rhizotrons (containers that force 2D growth conformation with transparent windows for observation) or transparent, artificial growth media. Although widely used, these methods generally result in root systems that vary considerably from those grown in natural soil conditions [7]. X-ray computed tomography is the primary method for 3D imaging of root systems grown in soil but is not without its limitations [8]. While X-rays show the soil structure and composition well, they are not an ideal tool for imaging water distribution in particular since there is very little contrast between water, plant roots and any other biological soil constituents. None of these hydrogen-rich constituents are resolved clearly and as a result it is difficult to differentiate between them in the image data produced.

Neutron imaging offers a solution as many of the imaging techniques are similar but the mechanisms by which neutrons interact with matter are very different and hence different elements, in particular light elements such as hydrogen, provide strong contrast in a neutron image [9]. A number of experiments have shown neutron imaging to be well suited to showing water dynamics, where X-ray imaging would have struggled [10-15]. Neutron imaging has its own limitations however: it is slower, less readily available and produces images of lower resolution when compared to equivalent X-ray techniques. Just as X-ray imaging cannot provide a good representation of all the materials in a plant sample, neutron imaging struggles to show the soil minerals and structure clearly.

Registration

Bi-modal datasets require registration to align the data from each modality. Although some cases have successfully used mutual information in the sample to achieve registration [16], in general it has been shown that, due to the complementary nature of the modalities, there is no guarantee that there will be similar local features in corresponding datasets (particularly with multi-phase images) and it is therefore difficult to find a good registration solution based on common features within a sample [9]. To overcome this difficulty, fiducial markers can be attached to a sample to aid in registration. A fiducial marker is an object placed within an image to be used as a point of reference. To register volumes using fiducial markers, at least three fiducial points must be selected in both the reference and target images so that the registration parameters can be found and a suitable transform applied. In the case of CT volume data, this is typically achieved through an affine transform.

48 Inevitably, there will be error in the registration process. Maurer et al. defined three types of error
49 that can occur when using fiducial points for registration [17]:

50 • Fiducial localisation error (FLE): the average error in locating the position of the fiducial
51 points. (Figure 1 (A))
52 • Fiducial registration error (FRE): the root mean square (RMS) error between corresponding
53 fiducial points after registration. (Figure 1 (B))
54 • Target registration error (TRE): the error between corresponding points other than the
55 fiducial points after registration. (Figure 1 (C))

56 Fitzpatrick and West built on these definitions by providing expressions for the expected FRE and
57 TRE errors in terms of the expected FLE and the set of fiducial points used (eq. 1) [18]. From this
58 expression, Wang and Song define an equation (eq. 2) to relate TRE to a particular distribution of
59 markers independently of FLE or FRE and propose a deterministic, optimisation method for
60 determining the quantity and layout of markers to minimise TRE at a point of interest r [19]. The
61 distance from r to each axis is donated as d_k, where $k = (1, 2, 3)$ and f_k is the RMS distance of all
62 fiducial points to the kth coordinate axis.

$$E\{TRE^2(r)\} \approx \frac{E\{FRE^2\}}{N-2}\left(1 + \frac{1}{3}\sum_{k=1}^{3}\frac{d_k^2}{f_k^2}\right) \qquad (eq.1)$$

63

$$TRE_M(r) = \frac{1}{N-2}\left(1 + \frac{1}{3}\sum_{k=1}^{3}\frac{d_k^2}{f_k^2}\right) \qquad (eq.2)$$

64

65

X-ray and neutron imaging equipment

67 This project is a pathfinder application for the new IMAT instrument at ISIS Neutron and Muon
68 Source. IMAT is a combined cold neutron imaging and diffraction instrument designed to take
69 advantage of the second ISIS target station to provide neutron radiography, neutron tomography,
70 energy-selective neutron imaging and spatially resolved diffraction scans [20]. The instrument
71 construction was completed in 2016 and since then IMAT has been running its imaging configuration
72 [21].

73 ISIS TS-2 is a short-pulse source which operates at 40 kW and delivers pulses at a rate of 10 Hz. IMAT
74 uses a cold (20 K), coupled liquid hydrogen moderator to slow the neutrons. A straight, 44 m
75 supermirror neutron guide transports the neutrons from the target to the experimental area. Three
76 choppers are placed within the guide to filter the beam. A T0 chopper removes fast neutrons and
77 gamma radiation, then a pair of double-disk choppers define the wavelength band to ensure there is
78 no frame overlap between successive neutron pulses. At the end of the guide is a pinhole selector
79 that allows the aperture diameter (D) to be varied between five values to define different L/D ratios,
80 where L (the distance from the aperture to the sample) is 10 m [22]. This results in a total flight path
81 of 56 m to the sample. Between the aperture and the sample, the beam travels through a 9 m
82 evacuated flight tube and is shaped by five sets of jaws [23]. The sample is placed on a combined
83 translation and rotation system that is rated for up to 1.5 tonnes.

84 IMAT has a variety of detectors but this work made use of IMAT's optical detector. This is based on a
85 Zyla sCMOS 4.2 Plus camera in an optical camera box with a field of view varying between 50 × 50
86 mm^2 and 200 × 200 mm^2 and acts as an integrating detector with a range of scintillators [24].

87 µ-VIS' modified Nikon/X-Tek HMX (225kVp) was used to produce the X-ray data for this work. This is
88 a customised, general purpose X-ray CT and radiographic inspection system. It can take samples up
89 to 300 mm in height although this is reduced to approximately 150 mm if the robotic sample
90 exchanger is used. The 225 kVp X-ray source can be configured for high resolution or high flux by

91 using different anodes and uses a PerkinElmer PE1621 flat panel detector to capture the image. The
92 detector is made up of a 2000 x 2000 matrix of amorphous silicon pixels with discrete gadolinium
93 oxysulphide scintillators.

Simulation

95 In order to determine the best configuration of fiducial markers before imaging the samples, a
96 simulation was conducted based on the method presented by Wang and Song [19]. The method was
97 adapted to the case where the sample is cylindrical and the registration is to be optimised over the
98 whole volume of the sample rather than at a single point of interest.

99 $TRE_M(r)$ is a dimensionless quantity that relates the expectation value of TRE to that of FRE at a point
100 r, for a given set of markers M. Potential marker locations were given by a grid of points on the
101 surface of the cylinder. By evaluating $TRE_M(r)$ for a set of points evenly distributed throughout the
102 volume and taking the RMS value, an estimate of the TRE_M value is calculated for the whole volume.
103 This means that TRE_M gives a measure of how well two volumes can be registered with a set of
104 markers M independently of the FLE and FRE.

105 The simulation was run for N = {4, …, 16}, where N is the number of fiducial markers, to establish
106 how many fiducial points should be used and how they should be distributed about the sample.
107 Figure 2 shows how the value of TRE_M falls as the number of fiducial markers is increased. The
108 significance of each marker to the accuracy of the registration also falls quickly as N is increased as
109 shown in figure 3. This was calculated by taking the RMS average of the change in TRE_M when each
110 marker is removed from M. This trend confirms that for a larger number of markers, each marker is
111 less significant so less error is introduced if a marker cannot be accurately located or used for the
112 registration.

113 Figure 4 shows the optimal distributions found by the simulation for N = 10, 16. A number of trends
114 can be observed from the distributions of markers for different values of N and applied to the
115 general distribution of fiducial markers around a cylinder.

116 The first clear pattern is that the markers are distributed evenly between the very top and the very
117 bottom of the sample – maximising the distance between the markers and the centre of the volume.
118 This is a simple principle to apply when attaching markers to the sample and also has practical
119 benefits for the imaging process since it means that the markers can be placed higher and lower
120 than the soil in the sample tube. This means that areas of photon or neutron starvation, that could
121 produce artefacts in the reconstructed data due to the markers, can be located away from the
122 region of interest as the soil sample will not fill the very top and bottom of the sample tube.

123 Another clear pattern is that the markers are placed on a 180° arc at the top and another
124 corresponding arc at the bottom rather than, say, alternating between the top and bottom of the
125 cylinder. The markers are also evenly distributed around the cylinder, ensuring that the centroid of
126 the fiducial points is close to the centre of the sample.

127 Following these results from the optimisation algorithm a number of particular distributions were
128 chosen to further evaluate these patterns. By evalutating distributions with an even distribution of
129 markers between the top and bottom it was found that this generates very similar results. When
130 compared to arcs at the top and bottom, with the same positions in X and Y, the results were equal
131 to 2 significant figures and the small variations at greater precision did not conclusively show either
132 arrangement to be consistently better than the other for all values of N. It seems reasonable that the
133 simulation gives arcs because it begins the optimisation with a small number of markers and adds
134 optimised markers iteratively up to the required total rather than started with N markers and
135 attempting to redistribute them all.

136 The optimal arrangements found by the simulation were compared to random arrangements to see
137 how significant the differences are. 1,500,000 unique, random arrangements were evaluated for

138   each value of N. Figure 5 shows the minimum, mean and maximum values from these tests as well
139   as the optimal values (as seen in Figure 2). Figure 5a shows that a poor arrangement can increase
140   the error by as much as an order of magnitude when very few markers are used. With higher
141   numbers of markers however it becomes clear that the variation between good and bad
142   arrangements becomes insignificant. Figure 5b shows the same data in the range where N varies
143   between 12 and 16. It can be seen that the optimal solutions found by the simulation are better than
144   any of the values found in the 1.5 million random arrnagements but not by a significant amount. On
145   average, a random distribution of N+1 markers will give better results than the optimal distribution
146   of N markers.

147   Equation 1 states that the expectation of target registration error squared will be proportional to the
148   FRE, the number of markers and the distribution of the markers. The simulation results show that
149   with only four markers the TRE can be reduced to half of the FRE and that it can be reduced to less
150   than a tenth of the FRE by using more than twelve points. Using a high number of markers makes a
151   clear improvement to the result and also allows for the potential loss of a point without seeing a
152   large drop in accuracy.

Materials and Methods
153
154   A set of samples were imaged using both X-ray and neutron tomography and then registered to test
155   the proposed registration scheme and demonstrate the complementarity of the two modalities for
156   further studies.

157   Cadmium was proposed as a suitable material for fiducial markers since it has a large attenuation
158   coefficient for both neutrons and X-rays, allowing easy segmentation in either modality. An initial
159   scan, to confirm the suitability of the sample tube and markers, showed that the cadmium produced
160   significant artefacts, primarily due to beam hardening and scattering. It was decided that the
161   artefacts could be reduced to a satisfactory level provided the marker size was minimised and there
162   were sufficient variations in the height of the markers to avoid streaking between two markers in a
163   slice. Smaller cadmium pieces were cut and a new sample tube was scanned to ensure these
164   changes were sufficient.

165   Once the sample tube and marker configuration were shown to be suitable for imaging, a set of
166   plants were grown and imaged using both IMAT and the HMX at to produce a set of complementary
167   volumes that could be used to develop and test registration techniques. Twenty lupine seeds were
168   placed in wet paper towels to germinate. After six days, eight seeds that had begun to sprout were
169   selected and transferred to the sample tubes. New sample tubes were introduced for this
170   experiment that were made from boron free quartz with an inner diameter of 14 mm and a wall
171   thickness of 1.5 mm. Each tube had a single fibreglass wick to draw water for the plant. Within the
172   tube the wick was surrounded by 1 tsp of sand with particle sizes between 1.18 mm and 0.6 mm. Soil
173   of the same particle size range was then used to fill the tube, covering the seed around 20 mm from
174   the top. Each sample had a different quantity or arrangement of fiducial markers, as listed in Table 1.
175   These were selected to allow the simulation results to be compared to measured data. Due to beam-
176   time limitations, samples 2 and 6 were not scanned. The samples were left to grow for five days
177   before the scans began. The neutron scans were conducted first over two days and the X-ray scans
178   were collected over the following two days.

179   The neutron scans were conducted using the optical camera with a 135 mm lens, this gave a FOV of
180   60 x 60 mm. A 60 μm ZnS/LiF scintillator with a surface area of 90 x 90 mm was used. The beam was
181   shaped using the 40 mm pinhole and the jaws were set from 40 mm to 70 mm to match the beam
182   profile to the FOV as closely as can be achieved without introducing artefacts. The samples were
183   positioned 15 mm from the detector and 964 projections were taken with an exposure time of 30 s
184   per projection. The projections were reconstructed using the filtered back projection algorithm in
185   Octopus Reconstruction versions 8.9.3.4 and 8.9.4.2 [25]. The X-ray scans were conducted in the

186 HMX at 80 keV and 87 μA. 1571 projections were taken with four frames and a 500 ms exposure
187 time. The projections were reconstructed using Nikon CT Pro 3D version 2.2.5386.22184.

188 Once the scans were reconstructed, registration was attempted by segmenting the cadmium pieces
189 and taking their centres as fiducial points, before finding and applying the affine transform to best
190 match these points. The cadmium centres were located using a threshold segmentation in
191 conjunction with FIJI's 3D Objects Counter [26]. An affine transform can be determined to match the
192 two point sets. This is achieved by removing the translation and scaling differences by centring the
193 two points sets and using orthogonal reduction before the rotation component is determined using
194 Horn's algorithm [27]. Once the rotation has been found, the scaling and translation components
195 can be determined easily [28]. After the transform was applied, the volumes were then cropped to
196 matching dimensions. In order not to discard the higher resolution data in the X-ray scan, the
197 neutron data was considered the target volume. As a result it was scaled and hence resampled at a
198 higher resolution than IMAT could have achieved.

Results

200 Figures 6 and 7 show example slices and volumes from the reconstructed data collected using
201 neutron and X-ray imaging respectively.

202 Following the registration process, the fiducial markers were then resegmented in each modality and
203 the new positions compared to give the FRE for each sample. This can be taken as a reasonable
204 indicator of registration accuracy in the case of an affine transform. The FRE values are shown in
205 Table 1. The mean FRE of sample 5 was so much higher than that of the other samples due to one
206 marker which was misaligned by 18.5575 voxels. The mean FRE without taking that marker into
207 account is only 4.5003, which is far closer to the typical FRE values produced by the other samples.
208 This error was introduced as a result of a large FLE for this marker in the X-ray data due to an
209 artefact. Figure 8 shows how the threshold segmentation detects an area far greater than that of the
210 cadmium piece due to the artefacts surrounding it. This increase in the volume of the segmented
211 marker pulls the measured centre away from the true value and perhaps more importantly away
212 from the position found in the complementary modality to which it is to be matched.

213 Figure 9 shows a slice from sample 8 after registration. In addition to the combined data, each
214 modality is shown separately. The side by side and overlaid comparison clearly shows the differences
215 in contrast and signal to noise ratio between the two modalities but also the accuracy of the
216 registration – in particular when observing the aluminium tape around the outside of the tube. This
217 image also allows the complementarity to be seen clearly. Not only does the neutron data show the
218 plant root with greater contrast than the X-ray data but it shows some of the soil particles that
219 appear in the X-ray data while omitting others. This means that the combined data can be used to
220 infer information about the different materials making up soil particles which could not be
221 distinguished using X-rays alone.

Discussion and Conclusions

223 The data collected in this experiment demonstrates the suitability of X-ray and neutron tomography
224 for multi-modal studies, particularly into plant soil systems. In addition we have shown that fiducial
225 markers and the registration algorithms used allow the data from the two modalities to be
226 registered accurately, overcoming a lack of clear mutual information in the sample, and it can be
227 seen that more information can be taken by combining techniques than could be collected from
228 either technique in isolation.

229 There is no correlation between the FRE of the samples and the number and distribution of fiducial
230 markers used. For example, sample 1 has the second lowest FRE but had the worst set of fiducial
231 markers since it had the fewest markers and their arrangement was close to co-linear. Sample 5 had
232 the greatest number of markers and therefore had the best set of fiducial points, but it showed the
233 worst FRE of all the samples. The product of the FRE and TRE_M values (Table 1) gives an estimate for

234 the TRE for each sample. The variation FRE is far more significant in this calculation than that of TRE_M
235 which shows that being able to accurately image and locate the markers is more important to the
236 overall registration accuracy than having the markers ideally distributed.

237 The higher FRE of sample 5 indicates that artefacts in the scans which affect the segmentation of the
238 fiducial markers are the greatest source of error in registration (fig 8). Cadmium's high attenuation
239 introduces artefacts and these have been shown to have a negative impact on the registration
240 accuracy such that the effect of marker arrangement could not be tested in detail. This suggests that
241 while it can be used as a fiducial marker material, it is not ideal. A material that would attenuate
242 both X-rays and neutrons less would result in reduced artefacts, leading to not only better scan data
243 but more accurate registration since large FLE values as a result of image artefacts have been shown
244 to be the primary contributor to FRE in the registered data.

245 Further studies are being planned that will test the suitability of other materials, such as borosilicate
246 as fiducial markers.

247 Movement and other changes in the samples can be observed in the registered results, as a result of
248 the time and travel between the two scans of each sample. In particular, the seedlings begin to
249 droop and the top layers of soil can move considerably between the two scans. This will be
250 addressed in future studies by booking time to conduct both scans at the same site with minimal
251 delays between them. In addition, these studies will integrate synchrotron X-ray imaging which will
252 improve the resolution of the data and allow more complex imaging techniques to be introduced.

References

253 1. Tilman, D., et al., *Global food demand and the sustainable intensification of agriculture.*
254 Proceedings of the National Academy of Sciences, 2011. **108**(50): p. 20260-20264.
255 2. Ray, D.K., et al., *Yield Trends Are Insufficient to Double Global Crop Production by 2050.* PLOS
256 ONE, 2013. **8**(6): p. e66428.
257 3. Atkinson, J.A., et al., *Uncovering the hidden half of plants using new advances in root*
258 *phenotyping.* Current Opinion in Biotechnology, 2019. **55**: p. 1-8.
259 4. Bishopp, A. and J.P. Lynch, *The hidden half of crop yields.* Nature Plants, 2015. **1**: p. 15117.
260 5. Herder, G.D., et al., *The roots of a new green revolution.* Trends in Plant Science, 2010.
261 **15**(11): p. 600-607.
262 6. Lynch, J.P., *Roots of the Second Green Revolution.* Australian Journal of Botany, 2007. **55**(5):
263 p. 493-512.
264 7. Kuijken, R.C.P., et al., *Root phenotyping: from component trait in the lab to breeding.* Journal
265 of Experimental Botany, 2015. **66**(18): p. 5389-5401.
266 8. Mairhofer, S., et al., *RooTrak: Automated Recovery of Three-Dimensional Plant Root*
267 *Architecture in Soil from X-Ray Microcomputed Tomography Images Using Visual Tracking.*
268 Plant Physiology, 2012. **158**(2): p. 561-569.
269 9. Kaestner, A.P., et al., *Bimodal Imaging at ICON Using Neutrons and X-rays.* Physics Procedia,
270 2017. **88**: p. 314-321.
271 10. Menon, M., et al., *Visualization of root growth in heterogeneously contaminated soil using*
272 *neutron radiography.* European Journal of Soil Science, 2007. **58**(3): p. 802-810.
273 11. Matsushima, U., et al., *Estimation of water flow velocity in small plants using cold neutron*
274 *imaging with D2O tracer.* Nuclear Instruments and Methods in Physics Research Section A:
275 Accelerators, Spectrometers, Detectors and Associated Equipment, 2009. **605**(1-2): p. 146-
276 149.
277 12. Moradi, A.B., et al., *Three-dimensional visualization and quantification of water content in*
278 *the rhizosphere.* New Phytologist, 2011. **192**(3): p. 653-663.
279 13. Warren, J.M., et al., *Neutron imaging reveals internal plant water dynamics.* Plant and Soil,
280 2013. **366**(1-2): p. 683-693.

281   14.   Zarebanadkouki, M., Y.X. Kim, and A. Carminati, *Where do roots take up water? Neutron*
282   *radiography of water flow into the roots of transpiring plants growing in soil.* New Phytol,
283   2013. **199**(4): p. 1034-44.

284   15.   Totzke, C., et al., *Capturing 3D Water Flow in Rooted Soil by Ultra-fast Neutron Tomography.*
285   Sci Rep, 2017. **7**(1): p. 6192.

286   16.   Kim, F., et al., *Characterizing partially saturated compacted-sand specimen using 3D Image*
287   *registration of high-resolution neutron and X-ray tomography.* Journal of Computing in Civil
288   Engineering, 2014. **29**(6): p. 04014096.

289   17.   Maurer, C.R., et al., *Registration of head volume images using implantable fiducial markers.*
290   IEEE Transactions on Medical Imaging, 1997. **16**(4): p. 447-462.

291   18.   Fitzpatrick, J.M., J.B. West, and C.R. Maurer, *Predicting error in rigid-body point-based*
292   *registration.* IEEE Transactions on Medical Imaging, 1998. **17**(5): p. 694-702.

293   19.   Wang, M. and Z. Song, *Improving target registration accuracy in image-guided neurosurgery*
294   *by optimizing the distribution of fiducial points.* The International Journal of Medical
295   Robotics and Computer Assisted Surgery, 2009. **5**(1): p. 26-31.

296   20.   Kockelmann, W., et al., *IMAT – A New Imaging and Diffraction Instrument at ISIS.* Physics
297   Procedia, 2013. **43**(Supplement C): p. 100-110.

298   21.   BURCA, G., et al., *Exploring the potential of neutron imaging for life sciences on IMAT.*
299   Journal of Microscopy. **0**(0).

300   22.   Burca, G., et al., *Modelling of an imaging beamline at the ISIS pulsed neutron source.* Journal
301   of Instrumentation, 2013. **8**(10): p. P10001-P10001.

302   23.   Kockelmann, W., et al., *Status of the Neutron Imaging and Diffraction Instrument IMAT.*
303   Physics Procedia, 2015. **69**: p. 71-78.

304   24.   Finocchiaro, V., et al., *The autofocusing system of the IMAT neutron camera.* Review of
305   Scientific Instruments, 2013. **84**(9): p. 093701.

306   25.   Dierick, M., B. Masschaele, and L. Van Hoorebeke, *Octopus, a fast and user-friendly*
307   *tomographic reconstruction package developed in LabView®.* Measurement Science and
308   Technology, 2004. **15**(7): p. 1366.

309   26.   Schindelin, J., et al., *Fiji: an open-source platform for biological-image analysis.* Nat Meth,
310   2012. **9**(7): p. 676-682.

311   27.   Horn, B.K., *Closed-form solution of absolute orientation using unit quaternions.* JOSA A,
312   1987. **4**(4): p. 629-642.

313   28.   Qu, J., L. Gong, and L. Yang, *A 3D point matching algorithm for affine registration.*
314   International Journal of Computer Assisted Radiology and Surgery, 2011. **6**(2): p. 229-236.

315   29.   West, J.B., et al., *Fiducial Point Placement and the Accuracy of Point-based, Rigid Body*
316   *Registration.* Neurosurgery, 2001. **48**(4): p. 810-817.

Figure 1. *The three types of registration errors: FLE, FRE and TRE. Based on Figure 1 of [29].*

Figure 2. *The change in target registration error as the number of fiducial points is increased.*

Figure 3. *The average contribution of a single marker to the target registration accuracy as the number of markers increases.*

Figure 4. *The optimal fiducial marker distributions suggested by the simulation for N = 10 (top) and N = 16 (bottom).*

Figure 5. *A comparison of the optimal marker distributions to the mean, maximum and minimum TRE_M values found in 1,500,000 random trials. 5a (top) shows the full range of N values. 5b (bottom) shows N = 12 – 16.*

Figure 6. *A slice and partial volume render from the neutron scan of sample 7.*

Figure 7. *A slice and partial volume render from the X-ray scan of sample 8.*

Figure 8. *Sample 5 had the worst registration accuracy despite having the most fiducial markers. This figure shows how an artefact prevents accurate segmentation (segmentation shown in red) of a cadmium piece, creating a large FLE for the corresponding fiducial marker.*

Figure 9. *A slice from sample 8 with the X-ray data on the left and in red and the neutron data on the right and in green. This slice shows the match of a fiducial marker, the accuracy of the registration and the complementarity of the modalities.*

Table 1. *The fiducial marker arrangements, FRE measurements and TRE_M values for each of the sample tubes that was scanned.*

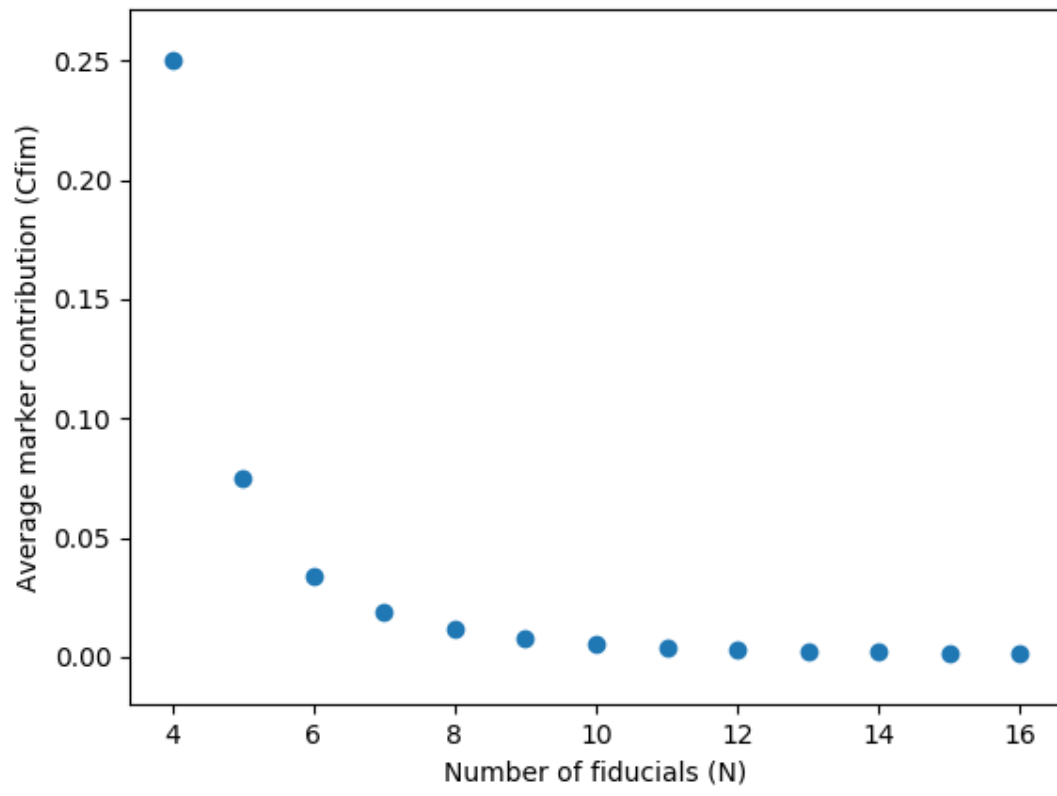*Figure 1*
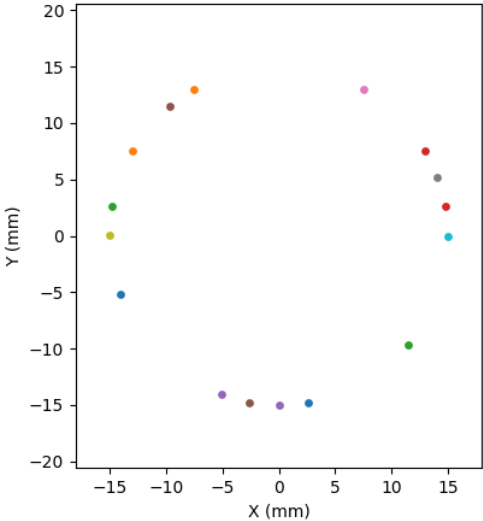

Figure2

Figure 2

317
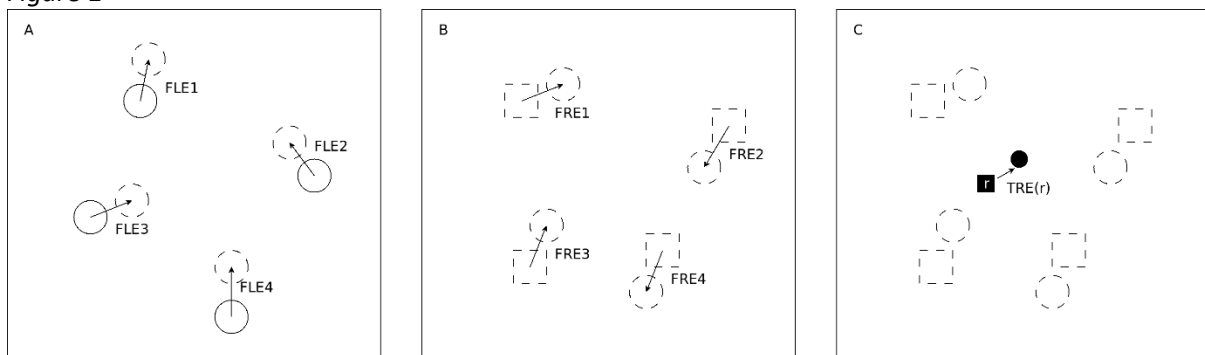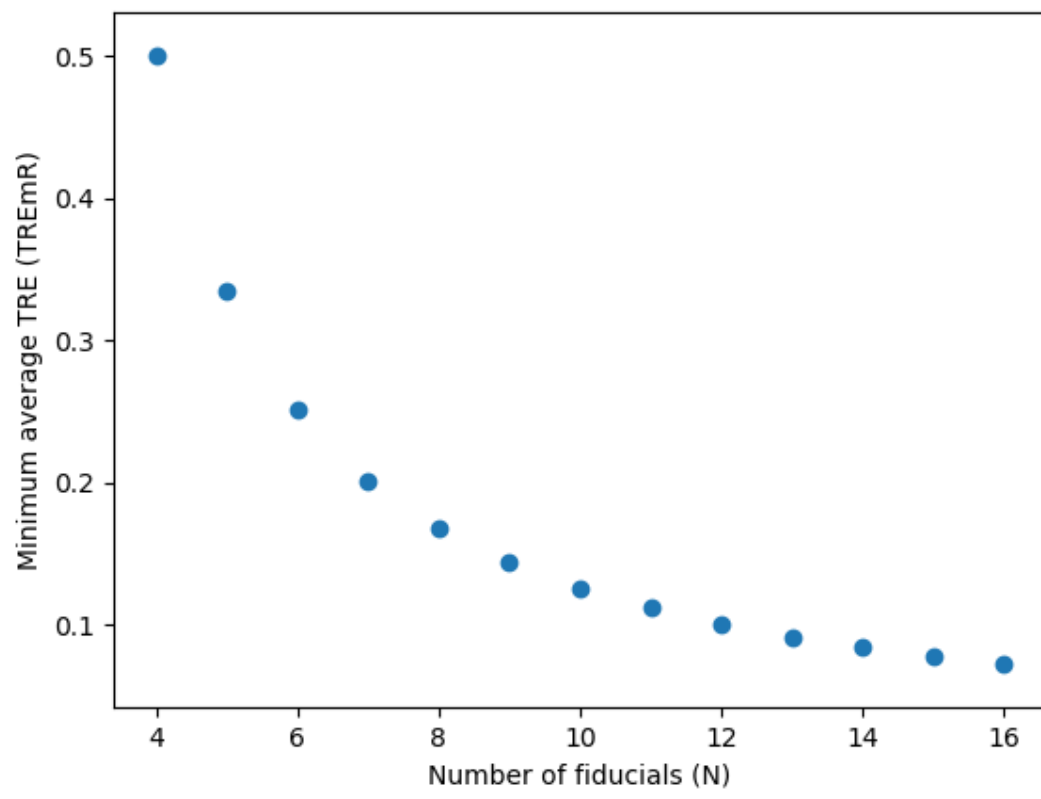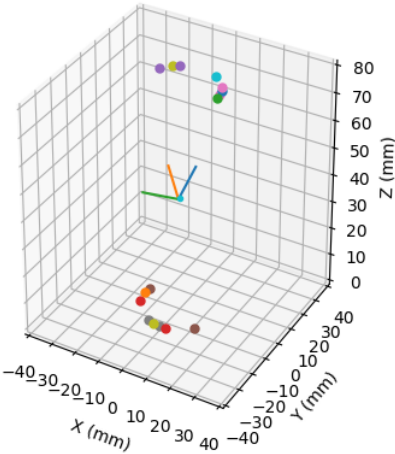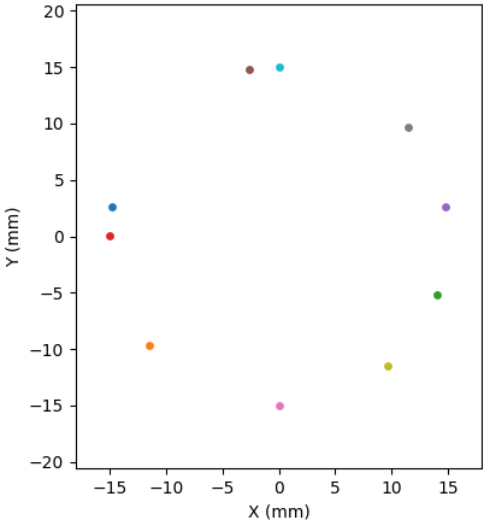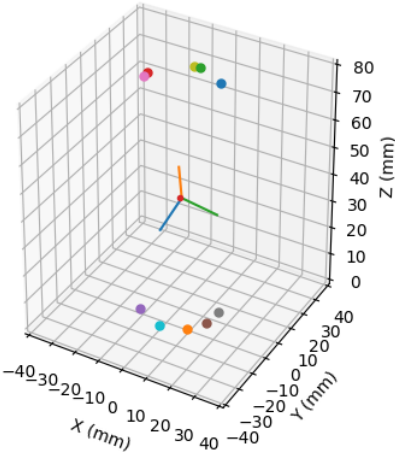
Figure 3

Figure 4

Figure 5

Figure 6

Figure 7

319   *Figure 8*
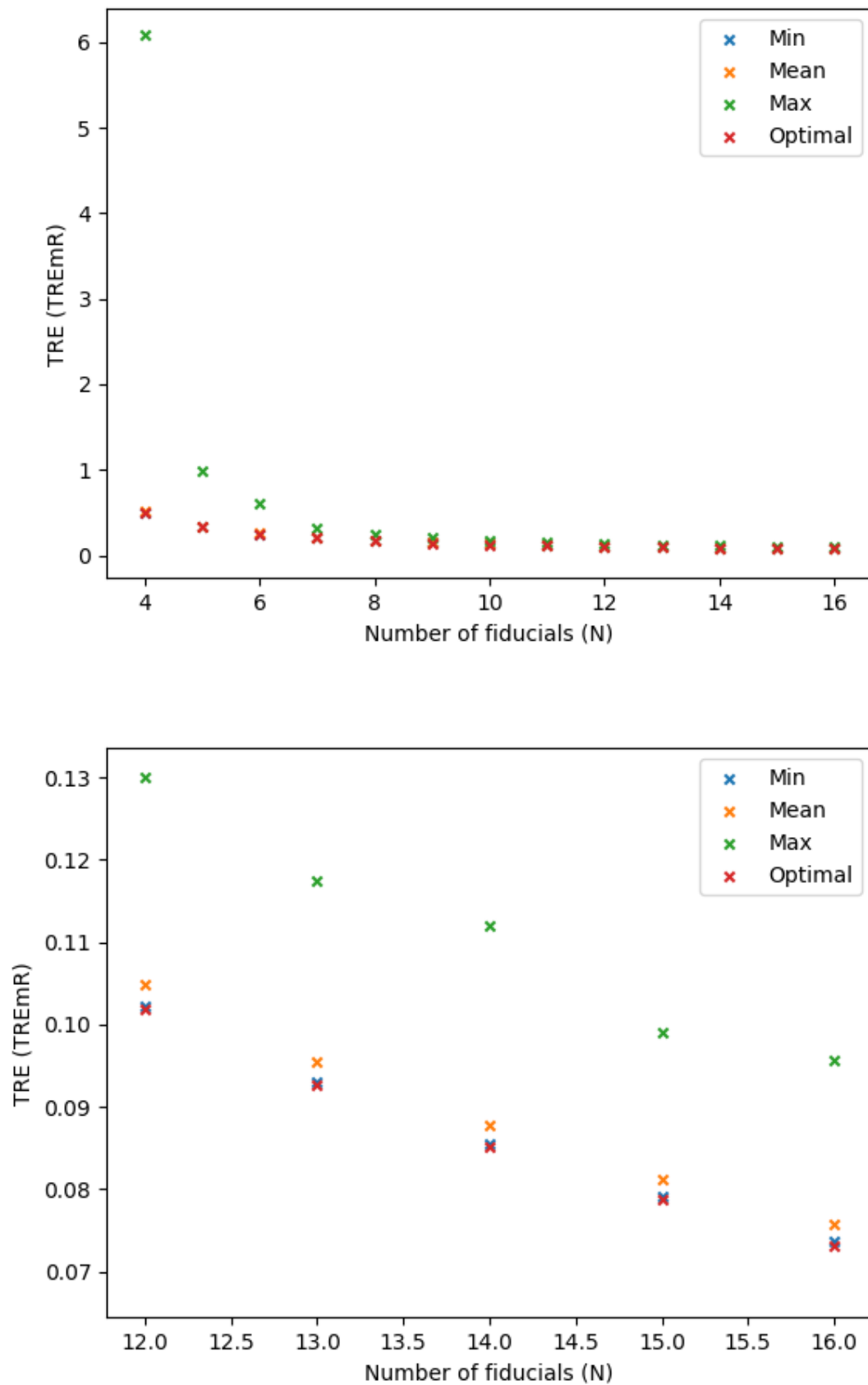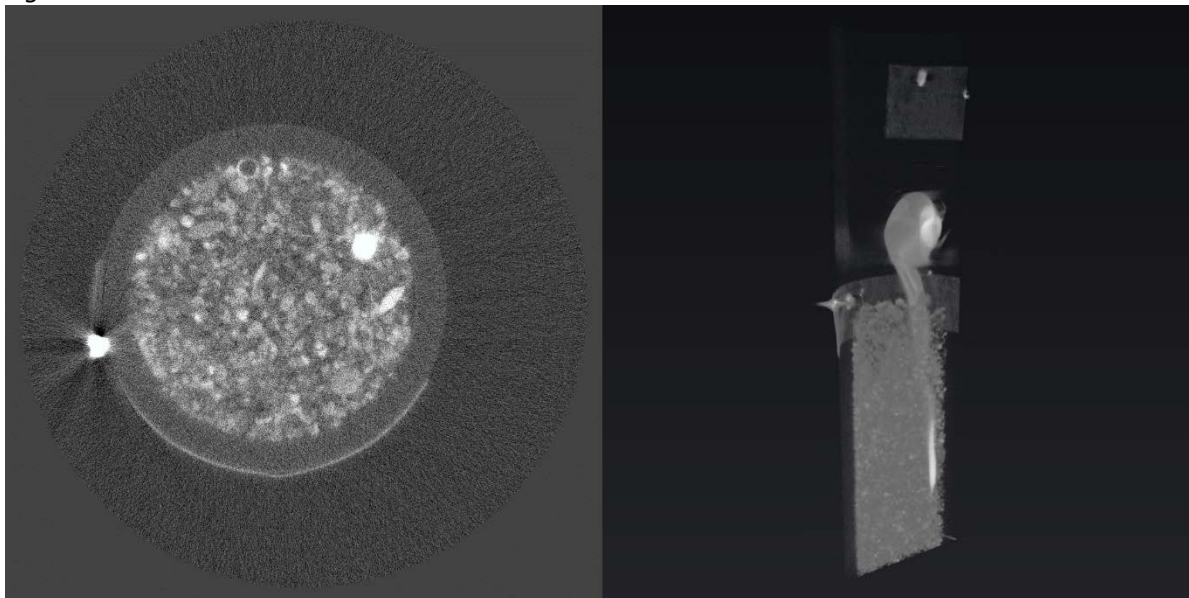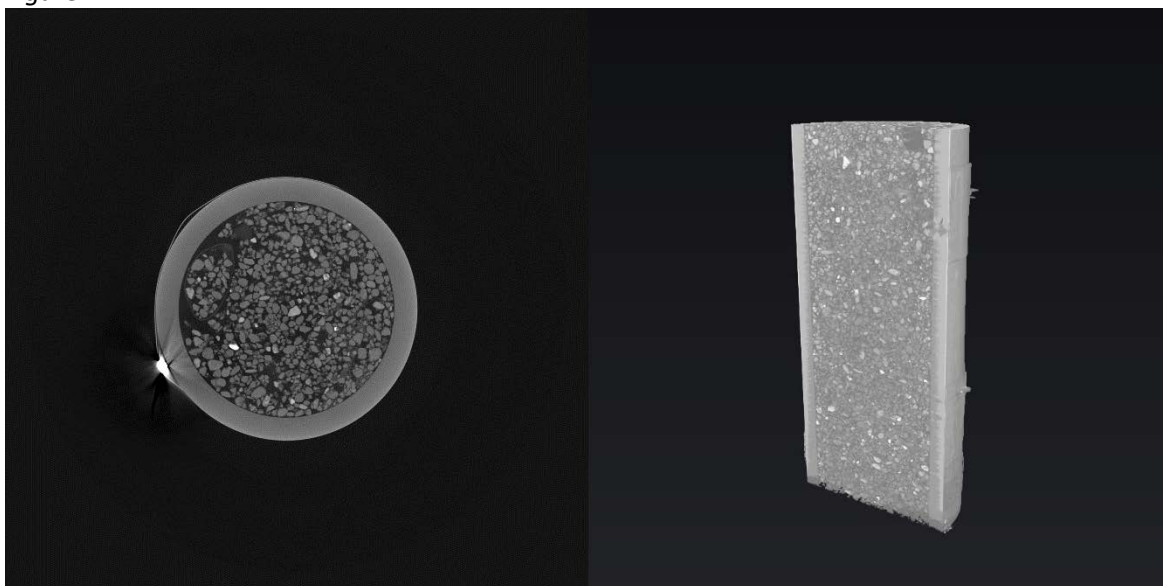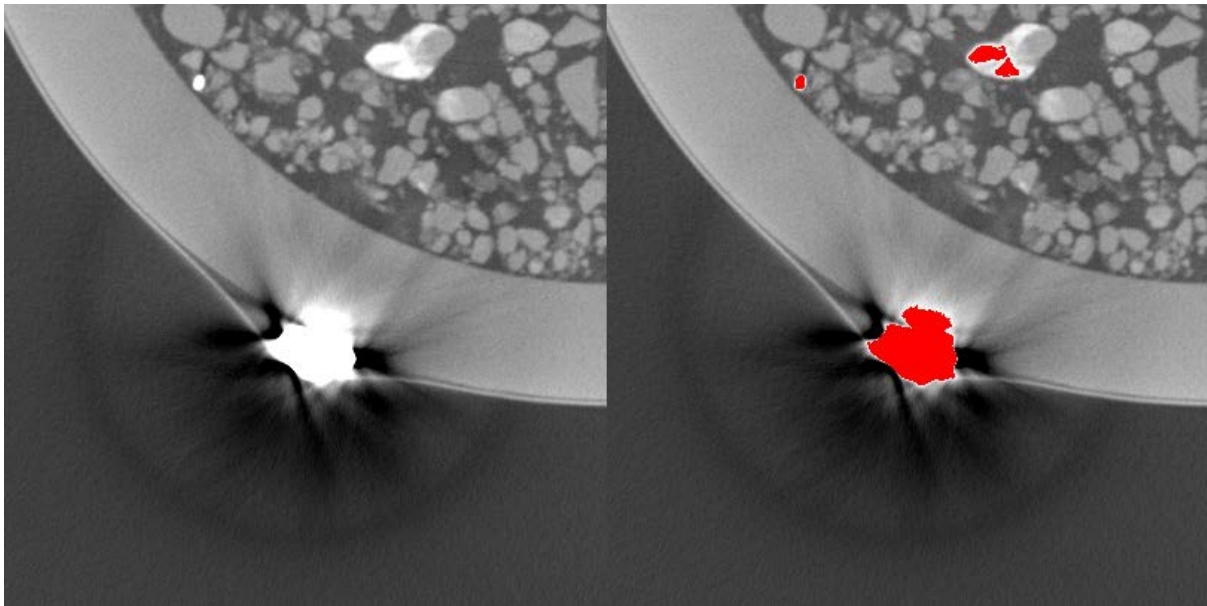
Figure 9
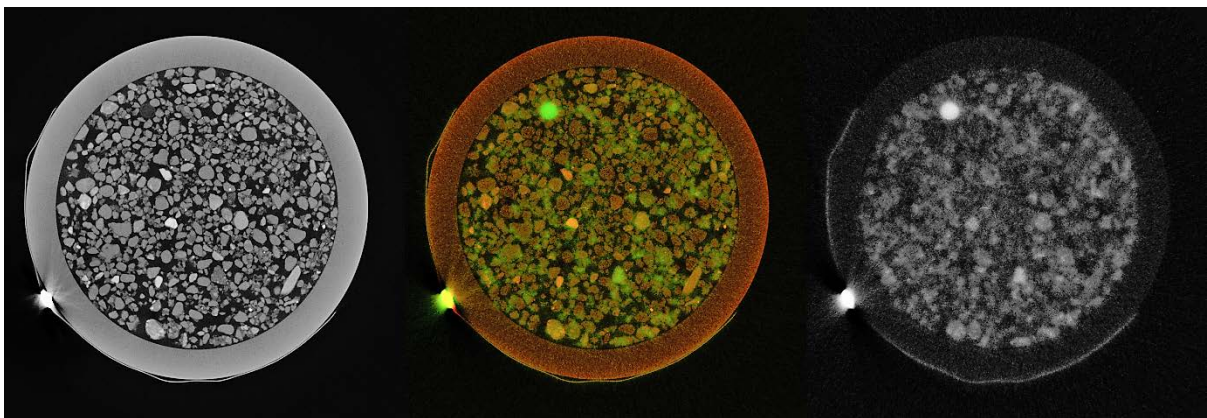
320   **Table 1**

SAMPLE	FIDUCIAL ARRANGEMENT	FRE	TRE$_M$	TRE (FRE × TRE$_M$)
1	5 markers in a vertical line	2.6618	0.3334	0.8874
3	6 markers in arcs at the top and bottom of the FOV	6.4916	0.2500	1.6229
4	8 markers in arcs at the top and bottom of the FOV	2.0335	0.1667	0.3390
5	10 markers in arcs at the top and bottom of the FOV	11.0246	0.1250	1.3781
7	9 markers in arcs at the top, middle and bottom of the FOV	4.3284	0.1429	0.6185
8	9 markers in arcs at the top, middle and bottom of the FOV	2.8543	0.1429	0.4079

321   **Table 1.** *The fiducial marker arrangements, FRE measurements and TRE$_M$ values for each of the*
322   *sample tubes that was scanned.*